Electrostatic Solitary Waves in the Solar Wind: Evidence for Instability at Solar Wind Current Sheets

David M. Malaspina,[1] David L. Newman,[2] Lynn B. Willson III,[3] Keith Goetz,[4] Paul J. Kellogg,[4] and Kris Kerstin[4]

[1]   A strong spatial association between bipolar electrostatic solitary waves (ESWs) and magnetic current sheets (CSs) in the solar wind is reported here for the first time. This association requires that the plasma instabilities (e.g., Buneman, electron two stream) which generate ESWs are preferentially localized to solar wind CSs. Distributions of CS properties (including shear angle, thickness, solar wind speed, and vector magnetic field change) are examined for differences between CSs associated with ESWs and randomly chosen CSs. Possible mechanisms for producing ESW-generating instabilities at solar wind CSs are considered, including magnetic reconnection.

1.   Introduction

[2]   Electrostatic solitary waves (ESWs) are often observed as coherent bipolar pulses in electric field data. They are observed in diverse plasma environments, including Earth's auroral region [*Ergun et al.*, 1998a], plasma sheet [*Pickett et al.*, 2009], magnetopause [*Matsumoto et al.*, 2003], magnetotail [*Matsumoto et al.*, 1994; *Andersson et al.*, 2009], cusp region [*Pickett et al.*, 2001], and bow shock [*Bale et al.*, 1998], as well as in the free solar wind [*Mangeney et al.*, 1999] and in association with interplanetary shocks [*Williams et al.*, 2005; *Wilson et al.*, 2007]. ESWs have also been generated in laboratory settings using an electron beam [*Lefebvre et al.*, 2010] and as a product of laboratory magnetic reconnection [*Fox et al.*, 2008; *Fox et al.*, 2012].

[3]   Extensive theoretical and simulation work (see [*Schamel*, 2012] and references therein) has shown that ESWs are well described as Bernstein–Greene–Kruskal (BGK) ion or electron phase space holes [*Bernstein et al.*, 1957] generated from beam, two-stream, or Buneman instabilities. For most ESW observations, potential sources of these instabilities have been identified. ESWs have been associated with ion and/or electron beams in laboratory

plasmas [*Lefebvre et al.*, 2010], beams generated by reflection at Earth's bow shock [*Bale et al.*, 1998], beams generated by reflection at shock ramps [*Williams et al.*, 2005], and by double layer related beams in the auroral region [*Ergun et al.*, 1998b] and magnetotail [*Andersson et al.*, 2009]. ESWs have also been associated with the modified two-stream instability (MTSI) at supercritical interplanetary shocks [*Wilson et al.*, 2010]. Counter streaming electron fluxes have been observed simultaneously with ESWs in Earth's plasma sheet [*Pickett et al.*, 2009], and ESW observations in the magnetotail, magnetopause, and in laboratory settings have been associated with reconnection events [*Cattell et al.*, 2005; *Matsumoto et al.*, 2003; *Fox et al.*, 2008]. ESWs previously observed in the solar wind have been identified by [*Mangeney et al.*, 1999] as weak double layers.

[4]   Many authors have observed ESWs in simulations of magnetic reconnection, including (1) ESWs generated by Buneman instability alone [*Drake et al.*, 2003; *Goldman et al.*, 2008], (2) ESWs generated by a two-step process transitioning from Buneman to Lower Hybrid and electron two-stream instability [*Che et al.*, 2010], and (3) ESWs generated by streaming instabilities at a variety of guide field strengths using realistic proton to electron mass ratios [*Lapenta et al.*, 2011]. All simulations have found ESWs localized to the reconnection separatrices, regions of high current and magnetic shear.

[5]   In this work, a strong spatial association is demonstrated between current sheets (CSs) and ESWs in the solar wind. The properties of solar wind ESWs and CSs are then examined, and possibilities for active beam, two-stream, or Buneman instabilities at solar wind CSs are discussed. The remainder of this paper is organized as follows. In section 2, the data set, detection algorithms for ESWs and CSs, as well as observed distributions of ESW and CS properties are presented. Possible sources for instabilities at solar

---

[1]Laboratory for Atmospheric and Space Physics, University of Colorado, Boulder, Colorado, USA.
[2]Center for Integrated Plasma Studies, University of Colorado at Boulder, Boulder, Colorado, USA.
[3]NASA Goddard Space Flight Center Code 672, Greenbelt, Maryland, USA.
[4]School of Physics and Astronomy, University of Minnesota, Minneapolis, Minnesota, USA.

Corresponding author: David M. Malaspina, Laboratory for Atmospheric and Space Physics, University of Colorado, Boulder, CO, USA. (David.Malaspina@colorado.edu)

wind CSs are discussed in section 3, and conclusions are presented in section 4.

2. Observations

[6] This study utilizes data from the spin-stabilized Wind spacecraft, orbiting the first Lagrange point $> 180 \, R_e$ Sunward of the terrestrial bow shock, from 1 January 2007 to 31 December 2007.

[7] Electric fields are studied using Wind Time Domain Sampler (Wind/TDS) waveform data [*Bougeret et al.*, 1995]. The data consist of 17 ms waveform captures of electric field data recorded at 120,000 samples per second by the Wind spin plane wire antennas operating as two orthogonal dipoles. The Wind spin plane is closely aligned with the ecliptic plane. The E_x wire booms are 100 m tip to tip, and the E_y wire booms are 14 m tip to tip. The noise level is higher on E_y due to the shorter antenna lengths. Due to instrumental limitations, only two orthogonal E signals can be telemetered to ground. These are nearly always E_x and E_y. The E_z component of the electric field is in general not telemetered to the ground.

[8] Magnetic fields are studied using the Wind/MAG fluxgate magnetometer data [*Lepping et al.*, 1995], recorded at 92 ms cadence. This data has gaps averaging less than 5 min per day. ESWs that occur during magnetic field data gaps are excluded from this study. Solar wind velocity, proton density, electron temperature, and proton temperature data are taken from 3 s moments of the Wind/3DP instrument [*Lin et al.*, 1995]. This data also has gaps that average a few minutes per day during the time period studied.

2.1. ESW Identification and Properties

[9] Over the 12 studied months, 4,393, TDS captures containing bipolar ESW waveforms are found out of 58,591 total TDS captures (7.5%). This corresponds to an average of ~160 TDS events and ~12 ESW events per day. ESW peak-to-peak amplitudes range from 0.1 mV/m to 8 mV/m with an average of 0.5 mV/m. The percentage of TDS captures containing ESWs is unexpectedly large given that phenomena associated with stronger electric fields such as Langmuir, whistler, and ion-acoustic waves (5–50 mV/m) or dust impacts (15–200 mV/m) are often preferentially selected by the TDS. This suggests that ESWs are far more ubiquitous in the solar wind than is observed. Note that each ESW TDS capture may contain one or more individual bipolar ESW pulses.

[10] To identify ESWs in the TDS data, events without sharp spikes are first excluded (those where the ratio $(\max|E|) / (< |E| >)$ is less than 4). Here, the time average is over the entire 17 ms duration of the Wind/TDS waveform capture. Then, waveforms with positive-peak to negative-peak ratio < 0.5 or > 1.5 are removed. These asymmetric waveforms are generally due to the impact of micron-sized dust particles (e.g., [*Zaslavsky et al.*, 2012]). The remaining waveforms are then examined by eye, and only those with isolated bipolar pulses (in either electric field component) are retained. For this study, isolated means that each bipolar pulse must be separated from other pulses or waves by at least one pulse width, defined as three times the distance between the positive and negative bipolar pulse peaks.

[11] Figure 1 shows a TDS waveform containing ESWs rotated into magnetic field aligned coordinates. Panel A (B) shows the electric field parallel, $E_\parallel$ (perpendicular, $E_\perp$), to the magnetic field. Vertical dashed lines in panels A and B indicate the portion of the waveform used to produce the hodogram in Panel C. This event was captured on 18 April 2007 at 07:36:19.363 when the interplanetary magnetic field lay nearly in the plane of the electric field booms (Bx = 1.62 nT, By = −1.60 nT, Bz = 0.08 nT, in GSE coordinates). The small angle between **B** and the XY GSE plane along with the larger than typical amplitude of this event ensures accurate determination of $E_\parallel$. The determination of $E_\perp$ is less accurate in this instance as only one dimension of $E_\perp$ can be measured. If the ESWs are interpreted as electron phase space holes (as argued below), then $E_\perp$ is expected to be symmetric about the magnetic field direction [*Muschietti et al.*, 2002], implying that the unmeasured $E_\perp$ component is likely to be of the same order as the measured $E_\perp$ component. This ESW is largely bipolar in the $E_\parallel$ direction and tripolar in the E_{perp} direction. Panel C of
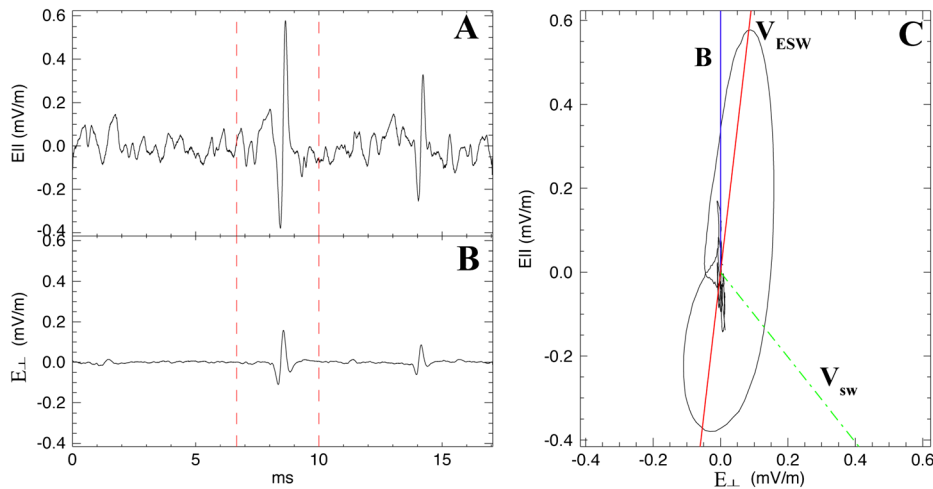

Figure 1. Electrostatic solitary wave electric field waveform capture rotated into magnetic field aligned coordinates. (A) Electric field parallel to **B**. (B) Electric field perpendicular to **B**. (C) Hodogram of parallel and perpendicular electric fields.

Figure 1 shows a hodogram of the electric field for this event. Blue solid, green dashed, and red solid lines show $\mathbf{B}$, v_{sw}, and v_{ESW}, which are the local magnetic field direction, solar wind direction, and bipolar axis of the ESW, respectively. The amplitude-symmetric (bipolar) axis of the hodogram (v_{ESW}) is closely aligned with $\mathbf{B}$ while the amplitude-asymmetric part of the waveform (tripolar) is close to perpendicular to $\mathbf{B}$. For this particular event, the longer E_x antennas were nearly aligned perpendicular to $\mathbf{B}$, while the shorter E_y antennas were aligned nearly parallel to $\mathbf{B}$.

[12] Tripolar signatures appear in $E_\perp$ because the Wind/TDS instrument is AC coupled and does not respond to electric fields below 120 Hz [*Bougeret et al.*, 1995]. Without response below 120 Hz, narrow unipolar pulses (< 5 ms) in the plasma will appear as tripolar pulses in the TDS. Wide unipolar pulses (> 5 ms) are reduced to ripples. Narrow bipolar pulses are not as strongly affected by the Wind/TDS AC coupling. Figure 2 illustrates the AC coupling effect. In each panel, the solid black curve shows a signal with response across all frequencies, while the dashed red curve represents the same signal with responses below 120 Hz removed. Clockwise from the upper left, the panels show a 2 ms bipolar pulse, an 8 ms bipolar pulse, an 8 ms unipolar pulse, and a 2 ms unipolar pulse. Note that narrow bipolar pulses largely retain their bipolar shape, while unipolar pulses are strongly altered. Consistent with this effect, narrow ESWs in the Wind data show tripolar E_{perp}, while wider ESWs show only ripples in $E_\perp$. We therefore interpret the tripolar pulse in $E_\perp$ as an AC-coupled unipolar pulse.

[13] In order to identify the observed ESWs as electron or ion phase space holes, a rough estimate of the hole velocity can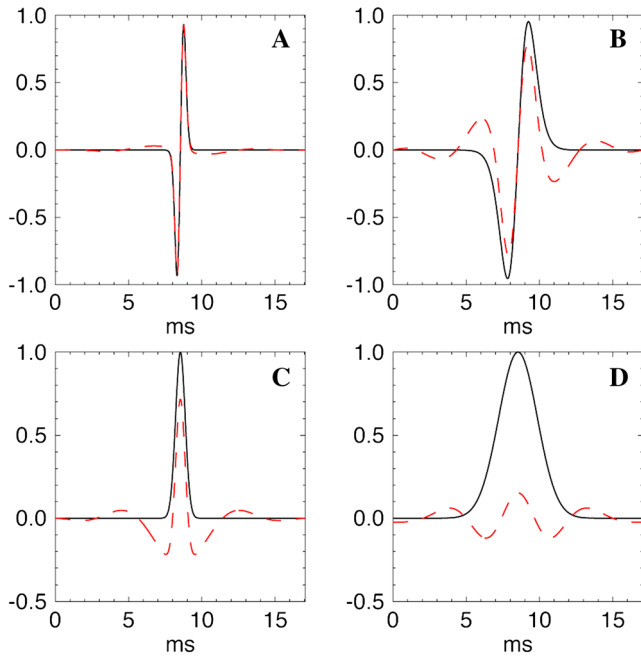 be made using ESW hodograms. Those ESWs traveling much faster than the solar wind velocity will move past the spacecraft primarily along the local magnetic field vector $\mathbf{B}$, therefore showing a bipolar electric field along $\mathbf{B}$ and a unipolar (tripolar in Wind/TDS data) electric field perpendicular to $\mathbf{B}$. ESWs traveling slower than the solar wind velocity (even if they propagate in the direction of $\mathbf{B}$) will move past the spacecraft primarily along the solar wind direction and therefore show a bipolar electric field along the solar wind velocity vector, $\mathbf{v_{sw}}$, and a unipolar (tripolar in Wind/TDS data) electric field perpendicular to $\mathbf{v_{sw}}$. ESWs traveling near v_{sw} along $\mathbf{B}$ will be bipolar along some direction between $\mathbf{B}$ and $\mathbf{v_{sw}}$ that depends on $\mathbf{v_{sw}}$ and the speed of the ESW along $\mathbf{B}$.

[14] For typical solar wind conditions (10 eV electrons, 400 km/s solar wind), $3v_{sw} \approx v_e$, where v_e is the electron thermal velocity. If the ESWs are moving much faster than v_{sw}, they must also be moving faster than v_e, consistent with identification of the ESWs as electron phase space holes (EH).

[15] To perform this estimate of ESW velocity, only ESWs where $\mathbf{B}$ lies within 5° of the Wind spin plane are used (636 events) to ensure that hodograms can be determined accurately with respect to $\mathbf{B}$. The hodogram of each ESW meeting this criteria was produced and the direction of the bipolar field determined by computing the principle axes of rotation for the hodogram shape. For a bipolar/unipolar structure, the principle axes of rotation are along the bipolar and unipolar directions (see Figure 1C). Hodograms subjected to the inertia tensor analysis are produced using only the highest amplitude isolated pulse in each TDS event to exclude the influence of adjacent wave or ESW structures.

[16] Figure 3 shows a scatter plot of θ_{ESW-V}, the angle between the direction of the bipolar axis of each ESW with respect to the solar wind direction, against θ_{B-V}, the angle between $\mathbf{B}$ and $\mathbf{v_{sw}}$. Here, θ_{B-V} is defined from 0° to 180°, while θ_{ESW-V} is defined from 0° to 90° because the direction of ESW propagation with respect to $\mathbf{B}$ has not yet been defined. Dashed lines show the expected behavior of points if ESW bipolar axes are oriented along $\mathbf{B}$.

[17] ESWs moving much slower than v_{sw} are convected past the spacecraft primarily by the solar wind flow and therefore will show bipolar character in the solar wind direction. These events will be clustered near $\theta_{ESW-V} = 0$ for any θ_{B-V}. ESWs moving much faster than v_{sw} are moving past the spacecraft primarily along the magnetic field direction and therefore will show bipolar character along the magnetic field direction,
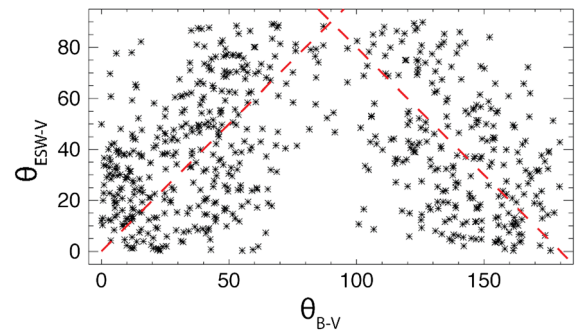

Figure 2. (A) and (B) show 2 ms and 8 ms bipolar pulses, respectively, as black solid traces. Red dashed traces show the bipolar pulses with power below 120 Hz removed. (C) and (D) show 2 ms and 8 ms unipolar pulses as black solid traces. Red dashed traces show the unipolar pulses with power below 120 Hz removed.

Figure 3. Angle between bipolar ESW axis and v_{sw} (θ_{ESW-V}) as a function of the angle between the local magnetic field B and v_{sw} (θ_{B-V}). Dashed lines indicate where $\theta_{ESW-V} = \theta_{B-V}$.

implying that $\theta_{ESW-V} = \theta_{B-V}$(red dashed lines). ESWs with velocity along the magnetic field of comparable magnitude to the solar wind convection velocity will appear scattered about $\theta_{ESW-V} = \theta_{B-V}$.

[18] Few ESWs appear to be moving slower than v_{sw}. Instead, most events are scattered about $\theta_{ESW-V} = \theta_{B-V}$, consistent with ESWs traveling along local magnetic field lines with velocities comparable to or much faster than $v_{sw} \approx 0.3v_e$). Figure 3 therefore suggests that solar wind ESWs are most likely EH, since their typical velocities are too large to be consistent with ion holes.

2.2. CS Identification

[19] In this study, CSs are identified using a modified version of the Partial Variance Increment (PVI) method of *Greco et al.* [2008]. In the PVI method, a CS is defined as a change in the magnetic field vector ($|\Delta\mathbf{B_{dt}}|$) that is large compared to typical fluctuations in $|\Delta\mathbf{B_{dt}}|$ over a scale size (dt) for a given interval of data. Specifically, the PVI method identifies CSs of scale dt as locations where the metric $PVI_{dt} = |\Delta\mathbf{B_{dt}}|/\sum_{\mathbf{dt}}$ exceeds a threshold value (γ). Here, $\Delta\mathbf{B_{dt}} = |\mathbf{B_{t+dt}} - \mathbf{B_t}|$ and $\sum_{dt} = \sqrt{<|\Delta B_{dt}|^2>}$, where the time average is performed over 1 day (approximately 9.4×10^5 magnetic field samples). PVI values exceeding γ correspond to strongly non-Gaussian magnetic field fluctuations. This study examines temporal scale sizes $0.092s < dt < 12s$.

[20] To identify CSs at multiple scales using the PVI method, the quantity PVI_{max} is created by taking the maximum PVI across all studied scales for each time point. All values of PVI_{max} below γ are then set to 0, leaving only strongly non-Gaussian fluctuations. Where more than one adjacent point has PVI_{max} exceeding γ, the largest PVI_{max} of those adjacent points is chosen to identify the CS. The PVI_{max} method efficiently identifies CSs of multiple scales in large data sets and returns the observed temporal duration of the CS (in sample rate units) by design, since each value of PVI_{max} is associated with a dt corresponding to the observed temporal duration of the CS signature.

[21] Each CS is assumed to be a locally planar three-dimensional structure with a normal determined by the cross product of the magnetic field vector one sample before the CS and one sample after the CS. This treatment is consistent with multi-spacecraft studies of solar wind CS geometry [*Knetter et al.*, 2004] that identified nearly all solar wind CSs as tangential discontinuities. The spatial width of each CS is calculated as $w_{CS} = (\mathbf{v}_{sw}\hat{n})dt$ where $\mathbf{v}_{sw}\hat{n}$ is the component of the solar wind velocity along the direction of the CS normal and dt is the CS temporal duration determined from PVI analysis.

[22] Here, we choose a threshold of $\gamma = 5$ to pick out only strongly non-Gaussian magnetic field fluctuations (*Greco et al.*, 2008). Adjusting this threshold to $\gamma = 3$ ($\gamma = 7$) results in more (fewer) magnetic structures identified as CSs. With fewer (more) CSs, the calculated distances between ESWs and CSs increase (decrease), yet the results presented in section 2.3 remain qualitatively the same as γ is varied about the nominal value of 5. That is, CSs are preferentially observed close to ESWs, and the CSs nearby ESWs do not show significantly different properties from randomly chosen CSs. See *Servidio et al.* [2011] for a further

discussion of CSs and reconnection event detection efficiency as a function of PVI threshold γ.

[23] Figure 4 demonstrates how a CS is identified by the PVI_{max} method. The top panel shows the magnetic field components in GSE coordinates at 92 ms resolution. The CS is indicated by two vertical dashed lines. The second panel shows PVI_{dt} for $0.092\ s < dt < 12\ s$ as overlaid color line plots. 130 values of dt are used in the analysis, in steps of 92 ms, but for clarity, only nine representative dt curves are plotted (dt = 0.736, 2.116, 3.496, 4.876, 6.256, 7.636, 9.016, 10.396, and 11.776 s). PVI_{max} is indicated by the heavy black line enveloping the colored line plots. Once $PVI_{max} < 5$ are removed, the largest value in the remaining "island" of PVI_{max} is chosen to represent the CS. The identified CS therefore has PVI_{max} = 8.24, which occurs for dt = 0.736 s at the location of the leftmost vertical dashed line in the top panel. The rightmost vertical dashed line is simply the location of largest PVI_{max} plus 0.736 s. 343,927 CSs are identified in the Wind magnetometer data during 2007 by the PVI_{max} method. This represents an average of 942 CSs identified per day.

2.3. Solitary Waves and CSs

[24] For each of the 4,393 ESW events, the CS closest to the position of Wind at the instant of ESW observation is identified. For clarity, these CSs are hereafter referred to as E-CSs. As a control sample, 4,113 randomly selected times in the magnetometer data are chosen (12 per day, less those locations that occurred during magnetometer data gaps). The CS closest to Wind at each randomly selected time is then identified. These CSs are referred to as R-CSs.
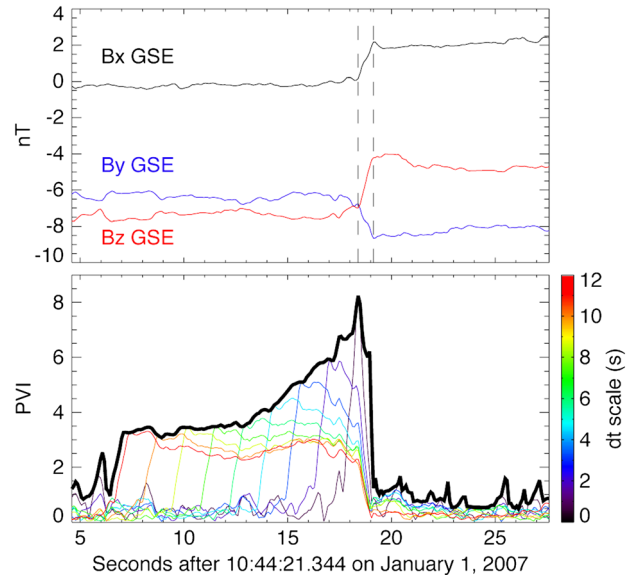

Figure 4. Top panel: GSE Magnetic field measured on 1 January 2007 near 10 h, 44 min, 21 s, 344 ms. Dashed lines indicate start and end of identified current sheet. Bottom panel, colored curves: Partial Variance Increment (PVI) for 9 of the 130 considered scales (dt) of step size 92 ms. Plotted scales are dt = 0.736, 2.116, 3.496, 4.876, 6.256, 7.636, 9.016, 10.396, and 11.776 s. Bottom panel, thick envelope curve: PVI_{max} at each time.

[25] The distance between Wind (a point) and each E-CS or R-CS (a plane) is calculated as the product of the component of the solar wind velocity normal to the CS surface and the temporal separation between the CS observation by Wind and either the time of ESW observation (for E-CSs) or the randomly selected time (for R-CSs). This assumes planar CSs moving past the spacecraft with the solar wind velocity. The thickness of each CS is taken into account in that distances are calculated with respect to the center of each CS.

[26] Figure 5 shows (1) the distribution of distances between Wind and E-CSs (black) and (2) the distribution of distances between Wind and R-CSs (red) for all of 2007. Each population has been normalized to 1. The primary plot shows distances up to 1.1×10^5km, while the inset plot shows distances up to 9×10^3km. From this data, it is evident that ESWs preferentially occur close to CSs. Further, Figure 5 shows that the probability of finding a CS near an ESW increases with decreasing distance to the nearest CS. Approximately 47% of all ESW observation locations occur within 6×10^3km of a CS, compared with only $\sim 17\%$ of the randomly chosen locations. Similar plots made using only data from any given month during 2007 show the same preference for ESWs to occur near CSs (plots not shown). Error bars on the inset plot represent counting uncertainties of $\pm\sqrt{N}$ where N is the number of events in a given bin.

[27] Figure 6 shows peak-to-peak ESW amplitude as a function of distance between Wind and E-CSs. The peak-to-peak amplitudes refer to the vector sum of the peak-to-peak amplitudes measured separately on the E_x and E_x orthogonal antennas. The data presented here have been normalized such that each point shows the average amplitude and distance for an equal number of ESW events (100 for each point). For example, the leftmost point shows the average amplitude and distance for the 100 ESWs that are closest to a CS. From this plot, one can see that average ESW amplitude decreases with
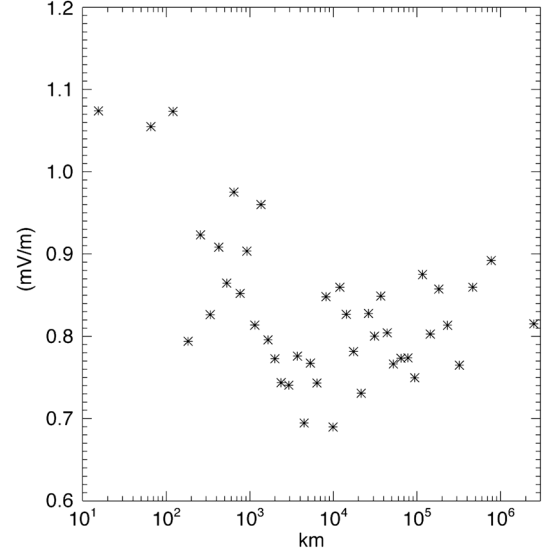

Figure 6. Average peak-to-peak ESW amplitude as a function of average ESW-to-current sheet distance for each 100 ESW events.

increasing distance from CSs. The average ESW amplitude decreases by about 1/2 over 6000 km in ESW to CS distance, while events beyond 6000 km do not show strong amplitude changes with increasing distance. However, these distant ESW events cannot be conclusively related to the nearest identified CS (see Figure 5).

[28] Figures 7–10 show distributions of shear angle, thickness, vector magnetic field change ($|\Delta B|$), and v_{sw} for E-CSs (black traces) and R-CSs (red traces). For these plots, only E-CS events with Wind-to-CS distances less than 6000 km are considered (2036 events). This distance restriction emphasizes differences between E-CSs and R-CSs by selecting only those distances where ESWs are more likely than
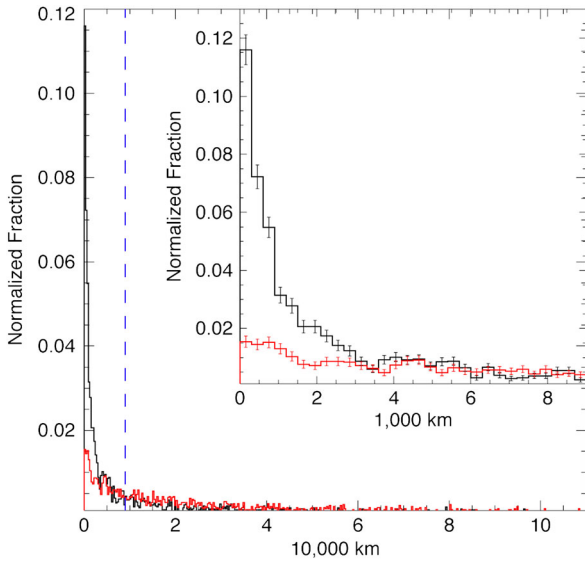

Figure 5. Distributions (normalized to 1) of distances between Wind and the closest current sheet for: ESW observation times (black trace) and randomly chosen observation times (red trace). Inset plot shows a close-up of short distances, indicated by the dashed line in the primary plot.
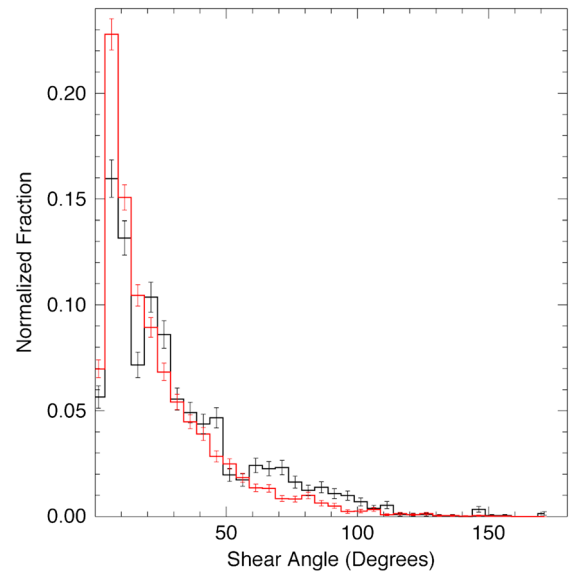

Figure 7. Distributions (normalized to 1) of current sheet shear angle for current sheets closest to all randomly chosen observation times (red trace) and current sheets within 6000 km of Wind when ESWs are observed (black trace).

Figure 8. Distributions (normalized to 1) of current sheet thickness for current sheets closest to all randomly chosen observation times (red trace) and current sheets within 6000 km of Wind when ESWs are observed (black trace).

Figure 9. Distributions (normalized to 1) of the magnitude of the vector magnetic field change for current sheets closest to all randomly chosen observation times (red trace) and current sheets within 6000 km of Wind when ESWs are observed (black trace).
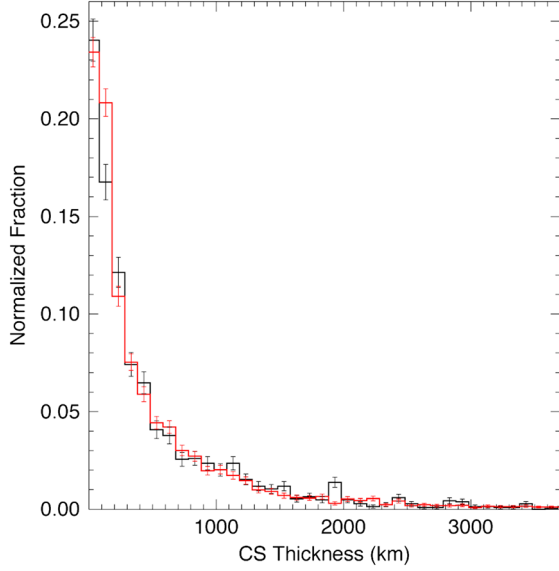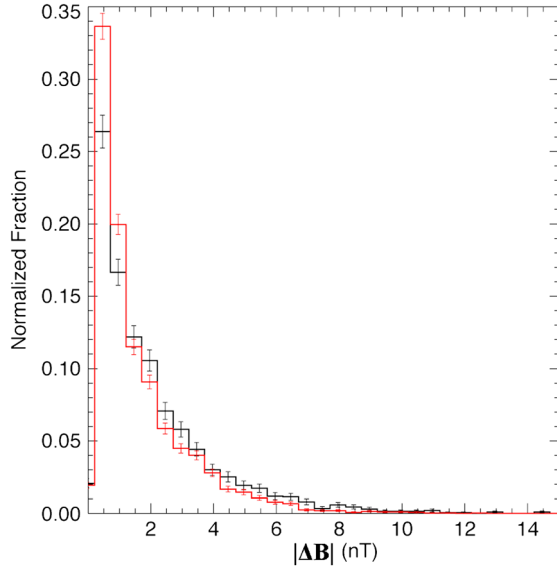
random to be observed near a CS (see Figure 5). Here, shear angle is defined as the angle through which the magnetic field rotates across a CS, and thickness is calculated assuming a three-dimensional locally planar CS moving with the solar wind velocity. Again, error bars represent counting uncertainties of $\pm\sqrt{N}$ for each bin are included.

[29] From Figures 7–10, one can see small differences between CS populations in that E-CSs are slightly more likely to have larger shear angles and larger $|\Delta\mathbf{B}|$ when compared to
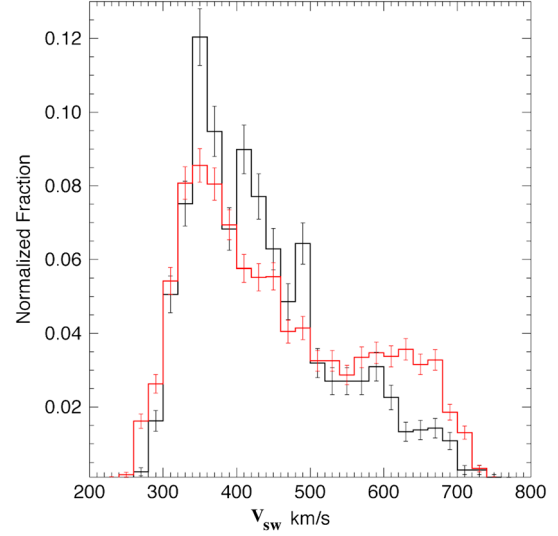

Figure 10. Distributions (normalized to 1) of v_{sw} at current sheets closest to all randomly chosen observation times (red trace) and current sheets within 6000 km of Wind when ESWs are observed (black trace).

R-CSs. Also, E-CSs are more likely than R-CSs be observed when $v_{sw} > 580$ km/s and E-CSs are less likely than R-CSs be observed when $v_{sw} < 580$ km/s.

3. Discussion

[30] BGK phase space holes are known to be generated by instabilities such as electron-electron two-steam or electron-ion Buneman instabilities. These instabilities can be localized to CSs due to currents supported by CS magnetic shear or because of magnetic reconnection somewhere along a given CS.

[31] CSs by definition contain a current (J) associated with the magnetic shear, given by $\nabla \times \mathbf{B} = \mu_0 \mathbf{J}$ across the CS. If strong enough, this CS current can directly drive a Buneman instability within the CS. To determine whether solar wind CSs at 1 AU have the correct order of magnitude of currents to drive ESWs by Buneman instability, one can define the CS current as:

$$\nabla \times \mathbf{B} = \mu_0 \mathbf{J} = \mu_0 n_i q_e (v_i - v_e) \hat{J} \qquad (1)$$

where the ion density n_i is used because quasi-neutrality is assumed, q_e is the fundamental charge, and v_i, v_e are the proton and electron thermal velocities. A Buneman-unstable distribution requires a minimum separation between proton and electron thermal distributions of $1.34 v_e$ to generate ESWs [*Buneman*, 1959] and greater drifts if non-thermal electron and ion populations are considered. For this order of magnitude calculation, $(v_i - v_e) = 2v_e$ is used. $\nabla \times \mathbf{B}$ can be written as

$$\left(\frac{\partial B_z}{\partial y} - \frac{\partial B_y}{\partial z}\right)\hat{x} - \left(\frac{\partial B_z}{\partial x} - \frac{\partial B_x}{\partial z}\right)\hat{y} + \left(\frac{\partial B_y}{\partial x} - \frac{\partial B_x}{\partial y}\right)\hat{z} \qquad (2)$$

[32] Where $\hat{x}$ and $\hat{y}$ are in the plane of the CS, and $\hat{z}$ is parallel with the CS normal. For a CS that is a tangential discontinuity, $B_z = 0$. For a CS that is locally planar, $\partial B_x/\partial y = \partial B_y/\partial x = 0$. Taking $B_y = 0$, equation (2) reduces to $\partial B_x/\partial z$,

which is approximately equal to the change in B_x across the width of the CS ($\Delta B_x/\Delta z$). With a CS shear angle of 180°, $\Delta B_x = 2B_x$, and the condition for driving a Buneman instability from CS magnetic shear alone becomes

$$v_e \leq \left(\frac{B_x}{\Delta z}\right)\left(\frac{1}{\mu_0 n_i q_e}\right). \tag{3}$$

[33] For typical 1 AU solar wind CS values $B_x \approx 9$nT, Δz 200km, and $n_i \approx 9$ cm^{-3}, the right-hand side of equation (3) becomes $\sim$45 km/s, 3.3 % of the typical solar wind electron thermal velocity (1,326 km/s for 10 eV electrons). Based on these values, a typical solar wind CS at 1 AU does not carry enough current to drive a Buneman instability. However, estimates of CS thickness and B_x across the CS at 1 AU come from the Wind/MAG fluxgate magnetometer measurements. The MAG data are low pass filtered and so by design cannot contain information about higher-frequency (potentially higher-amplitude) fluctuations.

[34] Interestingly, if one scales 1 AU CS values to solar wind at the closest perihelion of the future Solar Probe Plus mission, 8.5 Solar Radii (Rs) from the solar surface, B_x 2,100nT, $\Delta z \approx 2$km, $n_i \approx 4,022$ cm^{-3}, $T_e \approx 85$eV, and the right-hand side of equation (3) becomes 33 % of the local electron thermal speed. Under these conditions, a solar wind CS with a magnetic field fluctuation only a few times the nominal B-field strength can directly drive a Buneman instability capable of producing ESWs.

[35] Recent observations by [Osman et al., 2012] indicate that increased plasma temperatures and large PVI values are often observed in plasma that is near the thresholds of the mirror-mode, ion-cyclotron, and fire-hose instabilities. While Buneman is a small-scale instability, unlikely to act over large swaths of plasma, it can perhaps account for some of the dissipation of magnetic free energy at CSs. This would be especially relevant for exceptionally thin, small-scale CS where growth of ESWs and other Buneman-unstable waves would quickly saturate a CS-driven Buneman instability, lowering the current of the unstable portion of the CS, thereby reducing the magnetic shear that can be supported at that location. The generation of ion-gyroscale CSs by turbulent cascade in the solar wind (see [Greco et al., 2009] and references therein) could be one mechanism by which fine structures with Buneman-unstable magnetic shear are constantly regenerated, leading to the observation of ESW associated with CSs at 1 AU.

[36] If magnetic reconnection occurs along a given CS, Buneman or electron two-stream instabilities will likely be driven at the reconnection site [Drake et al., 2003; Che et al., 2010]. Simulations of magnetic reconnection often show the formation of bipolar ESWs along reconnection separatrices [Pritchett & Coroniti, 2004; Drake et al., 2005; Lapenta et al., 2011]. In fully three-dimensional reconnection at solar wind-like small-shear angle CSs (i.e., large guide field), ESWs are likely to exit the reconnection site along the guide field direction. Given the complex geometry of a three-dimensional reconnection site [Daughton et al., 2011] and the implied high speed of the observed ESWs ($\sim v_e$), one can easily imagine observing a reconnection-generated ESW near a CS that does not show the classic signs of reconnection (e.g., bifurcation of the CS, velocity jets [Gosling et al., 2005]).

[37] Additionally, reconnection simulations show that strong ESWs develop in density cavities along reconnection separatrices where the density may reach an order of magnitude below the ambient plasma density [Pritchett & Coroniti, 2004; Drake et al., 2005]. While Wind either cannot resolve these cavities or does not observe them due to its location far from the reconnection x-line when ESWs are observed, the data do not conclusively rule out ESW generation by reconnection-driven Buneman instability in the solar wind.

[38] Observationally, it is difficult to draw definitive conclusions about reconnection signatures of CSs near ESWs for two reasons. First, most CSs identified near ESWs are narrower than 6 s, the minimum amount of time required for Wind particle instruments to return two samples of full particle moment data. This makes it impossible to conclusively identify reconnection events by their outflow jets. Second, TDS waveform captures are triggered by high amplitude electric fields, not by reconnection events, and therefore electric field data coverage of identifiable reconnection events is sporadic. Ideally, one would first identify reconnection events by their magnetic signatures and reconnection jets and then examine electric field data for ESWs. Such a study is not practical because the bandwidth required to telemeter extended time coverage of high cadence electric field data exceeds the capabilities of current spacecraft.

[39] The property distributions of E-CSs examined in section 2.3 suggest a preference for reconnection at E-CSs compared to R-CSs. E-CSs are more likely to show larger shear angles as well as larger vector magnetic field changes, and preferentially appear in the slow solar wind ($v_{sw} < 580$km/s). This last property echoes observations showing that reconnecting CSs are rare in the high speed solar wind (> 550km/s) [Gosling et al., 2007; Gosling, 2007].

[40] Streaming instabilities are also known to generate ESWs. For example, ESWs are associated with double layers in the terrestrial aurora [Ergun et al., 1998b] and magnetotail [Ergun et al., 2009]. None of the Wind/TDS waveforms in this data set were unequivocally identified as double layers. Even so, this does not rule out the presence of double layers at CSs as double layers are expected to be rare compared to the phase space holes that they produce [Ergun et al., 2009].

[41] The MTSI between ions reflected by high mach number shocks and electrons can also lead to ESW generation [Matsukiyo & Scholer, 2006], but few of the identified CSs are also shocks.

[42] Langmuir waves, which are often generated by bump-on-tail electron beam instability, have been observed to occur in the solar wind coincident with magnetic discontinuities [Lin et al., 1996]. While [Lin et al., 1996] reported some Langmuir waves at individual discontinuities (25%), most Langmuir waves reported (75%) were associated with depressions in the overall magnetic field strength bounded by a pair of discontinuities, often called magnetic holes. Beam instabilities are thought to be excited at magnetic holes due to a combination of adiabatic motion and time-of-flight effects acting on strahl electrons as they traverse the bounding discontinuities [MacDowall et al., 1996; Briand et al., 2010]. However, few of the CSs with nearby ESWs identified in the current study are positively identified as magnetic holes.

[43] ESWs are also observed in the STEREO/TDS data. The twin STEREO spacecraft orbit the Sun at 1 AU, one

ahead and one behind the Earth. These two spacecraft have three orthogonal 6 m electric field sensors operating as monopoles. Electric field data can be obtained from the potential difference between the electrostatic center of a given sensor and the spacecraft body, though the effective length of these antennas is only 1 m, much shorter and therefore much less sensitive than the electric field sensors on Wind. STEREO carries an improved version of the Wind/TDS receiver [*Bougeret et al.*, 2008] and is capable of recording data from all three orthogonal sensors to make waveform captures of 65 ms (sampled at 256 KS/s) or 130 ms (sampled at 125 kS/s). The STEREO electric field sensors are also AC coupled with little response below a few 10's of Hz.

[44] ESWs are observed in STEREO/TDS data infrequently due to two effects: (1) The STEREO antennas are much shorter than the Wind antennas and therefore much less able to resolve the low amplitude electric fields of typical solar wind ESWs (0.5 mV/m). (2) The STEREO/TDS triggered data collection is dominated by dust impact waveforms [*Zaslavsky et al.*, 2012] to such a degree that only a small portion of the data returned to Earth is free of dust spike contamination. Even with these limitations, one can occasionally find large amplitude ESWs (> 2 mV/m) in the STEREO/TDS data.

[45] The advantage of STEREO/TDS data is the availability of all three components of the electric field vector. Examining the three-dimensional electric field structure of 12 STEREO/TDS ESW events, it is found that these structures have bipolar $E_\parallel$ and tripolar $E_\perp$ morphology, exactly as those observed by the Wind/TDS when **B** was in the Wind spin plane. Also, all 12 identified STEREO/TDS ESWs were observed within 4000 km of solar wind CSs.

4. Conclusions

[46] This work used Wind spacecraft data to examine bipolar ESWs in the solar wind, finding that (1) the probability of observing ESWs increases with decreasing distance to magnetic discontinuities (CSs) at 1 AU. (2) Solitary wave amplitudes are larger closer to CSs. (3) Polarization data suggests that the solitary waves are mostly electron phase space holes. (4) Distributions of the properties of CSs with nearby solitary waves and those of randomly chosen CSs are not strongly different.

[47] Based on these observations, we conclude that an instability capable of producing ESWs is active at CSs in the solar wind at 1 AU. Possible instabilities include beam, Buneman, and two stream. As far as it is possible to determine from the data examined in this study, solar wind CSs are not observed to support enough current to directly drive Buneman instabilities, and no observational evidence for beam instabilities was discovered. Buneman or two-stream instability driven by magnetic reconnection may generate the observed solitary waves, but the properties of CSs with nearby solitary waves only suggest reconnection and offer no unequivocal evidence.

[48] The observation of solitary waves at solar wind CSs requires an instability to be active at CSs throughout the free solar wind. In the case of magnetic-shear driven Buneman or reconnection-driven Buneman or two stream, such instabilities may indicate the conversion of magnetic energy into plasma kinetic energy localized to solar wind CSs, a process suggested by turbulence studies.

References

Andersson, L., et al. (2009), New features of electron phase space holes observed by the THEMIS Mission, *Phys. Rev. Lett.*, *102*(22), 225004, doi:10.1103/PhysRevLett.102.225004.
Bale, S. D., P. J. Kellogg, D. E. Larson, R. P. Lin, K. Goetz, and R. P. Lepping (1998), Bipolar electrostatic structures in the shock transition region: Evidence of electron phase space holes, *Geophys. Res. Lett.*, *25*, 2929–2932, doi:10.1029/98GL02111.
Bernstein, I. B., J. M. Greene, and M. D. Kruskal (1957), Exact Nonlinear Plasma Oscillations, *Phys. Rev.*, *108*, 546–550, doi:10.1103/PhysRev.108.546.
Bougeret, J., et al. (1995), Waves: The radio and plasma wave investigation on the wind spacecraft, *Space Sci. Rev.*, *71*, 231–263, doi:10.1007/BF00751331.
Bougeret, J. L., et al. (2008), S/WAVES: The radio and plasma wave investigation on the STEREO Mission, *Space Sci. Rev.*, *136*, 487–528, doi:10.1007/s11214-007-9298-8.
Briand, C., J. Soucek, P. Henri, and A. Mangeney (2010), Waves at the electron plasma frequency associated with solar wind magnetic holes: STEREO/Cluster observations, *J. Geophys. Res.*, *115*, A12113, doi:10.1029/2010JA015849.
Buneman, O. (1959), Dissipation of currents in ionized media, *Phys. Rev.*, *115*, 503–517, doi:10.1103/PhysRev.115.503.
Cattell, C., et al. (2005), Cluster observations of electron holes in association with magnetotail reconnection and comparison to simulations, *J. Geophys. Res. Space Phys.*, *110*, A01211, doi:10.1029/2004JA010519.
Che, H., J. F. Drake, M. Swisdak, and P. H. Yoon (2010), Electron holes and heating in the reconnection dissipation region, *Geophys. Res. Lett.*, *37*, L11105, doi:10.1029/2010GL043608.
Daughton, W., V. Roytershteyn, H. Karimabadi, L. Yin, B. J. Albright, B. Bergen, and K. J. Bowers (2011), Role of electron physics in the development of turbulent magnetic reconnection in collisionless plasmas, *Nat. Phys.*, *7*, 539–542, doi:10.1038/nphys1965.
Drake, J. F., M. Swisdak, C. Cattell, M. A. Shay, B. N. Rogers, and A. Zeiler (2003), Formation of electron holes and particle energization during magnetic reconnection, *Science*, *299*, 873–877, doi:10.1126/science.1080333.
Drake, J. F., M. A. Shay, W. Thongthai, and M. Swisdak (2005), Production of energetic electrons during magnetic reconnection, *Phys. Rev. Lett.*, *94*(9), 095001, doi:10.1103/PhysRevLett.94.095001.
Ergun, R. E., C. W. Carlson, J. P. McFadden, F. S. Mozer, L. Muschietti, I. Roth, and R. J. Strangeway (1998a), Debye-scale plasma structures associated with magnetic-field-aligned electric fields, *Phys. Rev. Lett.*, *81*, 826–829, doi:10.1103/PhysRevLett.81.826.
Ergun, R. E., et al. (1998b), FAST satellite observations of large-amplitude solitary structures, *Geophys. Res. Lett.*, *25*, 2041–2044, doi:10.1029/98GL00636.
Ergun, R. E., et al. (2009), Observations of double layers in Earth's plasma sheet, *Phys. Rev. Lett.*, *102*(15), 155002, doi:10.1103/PhysRevLett.102.155002.
Fox, W., M. Porkolab, J. Egedal, N. Katz, and A. Le (2008), Laboratory observation of electron phase-space holes during magnetic reconnection, *Phys. Rev. Lett.*, *101*(25), 255003, doi:10.1103/PhysRevLett.101.255003.
Fox, W., M. Porkolab, J. Egedal, N. Katz, and A. Le (2012), Observations of electron phase-space holes driven during magnetic reconnection in a laboratory plasma, *Phys. Plasma*, *19*(3), 032,118, doi:10.1063/1.3692224.
Goldman, M. V., D. L. Newman, and P. Pritchett (2008), Vlasov simulations of electron holes driven by particle distributions from PIC reconnection simulations with a guide field, *Geophys. Res. Lett.*, *35*, L22109, doi:10.1029/2008GL035608.
Gosling, J. T. (2007), Observations of magnetic reconnection in the turbulent high-speed solar wind, *Astrophys. J. Lett.*, *671*, L73–L76, doi:10.1086/524842.
Gosling, J. T., R. M. Skoug, D. J. McComas, and C. W. Smith (2005), Direct evidence for magnetic reconnection in the solar wind near 1 AU, *J. Geophys. Res.*, *110*, A01107, doi:10.1029/2004JA010809.
Gosling, J. T., T. D. Phan, R. P. Lin, and A. Szabo (2007), Prevalence of magnetic reconnection at small field shear angles in the solar wind, *Geophys. Res. Lett.*, *34*, L15110, doi:10.1029/2007GL030706.
Greco, A., P. Chuychai, W. H. Matthaeus, S. Servidio, and P. Dmitruk (2008), Intermittent MHD structures and classical discontinuities, *Geophys. Res. Lett.*, *351*, L19,111, doi:10.1029/2008GL035454.

Greco, A., W. H. Matthaeus, S. Servidio, P. Chuychai, and P. Dmitruk (2009), Statistical analysis of discontinuities in solar wind ACE data and comparison with intermittent MHD turbulence, *Astrophys. J. Lett.*, *691*, L111–L114, doi:10.1088/0004-637X/691/2/L111.

Knetter, T., F. M. Neubauer, T. Horbury, and A. Balogh (2004), Four-point discontinuity observations using cluster magnetic field data: A statistical survey, *J. Geophys. Res.*, *109*, A06,102, doi:10.1029/2003JA010099.

Lapenta, G., S. Markidis, A. Divin, M. V. Goldman, and D. L. Newman (2011), Bipolar electric field signatures of reconnection separatrices for a hydrogen plasma at realistic guide fields, *Geophys. Res. Lett.*, *38*, L17104, doi:10.1029/2011GL048572.

Lefebvre, B., L.-J. Chen, W. Gekelman, P. Kintner, J. Pickett, P. Pribyl, S. Vincena, F. Chiang, and J. Judy (2010), Laboratory measurements of electrostatic solitary structures generated by beam injection, *Phys. Rev. Lett.*, *105*(11), 115001, doi:10.1103/PhysRevLett.105.115001.

Lepping, R. P., et al. (1995), The wind magnetic field investigation, *Space Sci. Rev.*, *71*, 207–229, doi:10.1007/BF00751330.

Lin, N., P. J. Kellogg, R. J. MacDowall, B. T. Tsurutani, and C. M. Ho (1996), Langmuir waves associated with discontinuities in the solar wind: a statistical study., *Astron. Astrophys.*, *316*, 425–429.

Lin, R. P., et al. (1995), A three-dimensional plasma and energetic particle investigation for the wind spacecraft, *Space Sci. Rev.*, *71*, 125–153, doi:10.1007/BF00751328.

MacDowall, R. J., N. Lin, P. J. Kellogg, A. Balogh, R. J. Forsyth, and M. Neugebauer (1996), Langmuir waves in magnetic holes: source mechanism and consequences, in *American Institute of Physics Conference Series*, *American Institute of Physics Conference Series*, vol. 382, edited by D. Winterhalter, J. T. Gosling, S. R. Habbal, W. S. Kurth, & M. Neugebauer, pp. 301–304, doi:10.1063/1.51486.

Mangeney, A., et al. (1999), WIND observations of coherent electrostatic waves in the solar wind, *Ann. Geophys.*, *17*, 307–320, doi:10.1007/s005850050760.

Matsukiyo, S., and M. Scholer (2006), On microinstabilities in the foot of high Mach number perpendicular shocks, *J. Geophys. Res.*, *111*, A06104, doi:10.1029/2005JA011409.

Matsumoto, H., H. Kojima, T. Miyatake, Y. Omura, M. Okada, I. Nagano, and M. Tsutsui (1994), Electrotastic Solitary Waves (ESW) in the magnetotail: BEN wave forms observed by GEOTAIL, *Geophys. Res. Lett.*, *21*, 2915–2918, doi:10.1029/94GL01284.

Matsumoto, H., X. H. Deng, H. Kojima, and R. R. Anderson (2003), Observation of Electrostatic Solitary Waves associated with reconnection on the dayside magnetopause boundary, *Geophys. Res. Lett.*, *30*(6), 1326, doi:10.1029/2002GL016319.

Muschietti, L., I. Roth, C. W. Carlson, and M. Berthomier (2002), Modeling stretched solitary waves along magnetic field lines, *Nonlinear Processes Geophys.*, *9*, 101–109.

Osman, K. T., W. H. Matthaeus, B. Hnat, and S. C. Chapman (2012), Kinetic signatures and intermittent turbulence in the solar wind plasma, *Phys. Rev. Lett.*, *108*(26), 261103, doi:10.1103/PhysRevLett.108.261103.

Pickett, J. S., J. R. Franz, J. D. Scudder, J. D. Menietti, D. A. Gurnett, G. B. Hospodarsky, R. M. Braunger, P. M. Kintner, and W. S. Kurth (2001), Plasma waves observed in the cusp turbulent boundary layer: An analysis of high time resolution wave and particle measurements from the Polar spacecraft, *J. Geophys. Res.*, *106*, 19,081–19,100, doi:10.1029/2000JA003012.

Pickett, J. S., et al. (2009), Electrostatic solitary waves in current layers: from Cluster observations during a super-substorm to beam experiments at the LAPD, *Nonlinear Processes Geophys.*, *16*, 431–442.

Pritchett, P. L., and F. V. Coroniti (2004), Three-dimensional collisionless magnetic reconnection in the presence of a guide field, *J. Geophys. Res. (Space Physics)*, *109*, A01220, doi:10.1029/2003JA009999.

Schamel, H. (2012), Cnoidal electron hole propagation: Trapping, the forgotten nonlinearity in plasma and fluid dynamics, *Phys. Plasmas*, *19* (2), 020,501, doi:10.1063/1.3682047.

Servidio, S., A. Greco, W. H. Matthaeus, K. T. Osman, and P. Dmitruk (2011), Statistical association of discontinuities and reconnection in magnetohydrodynamic turbulence, *J. Geophys. Res. (Space Physics)*, *116*, A09102, doi:10.1029/2011JA016569.

Williams, J. D., L.-J. Chen, W. S. Kurth, D. A. Gurnett, M. K. Dougherty, and A. M. Rymer (2005), Electrostatic solitary structures associated with the November 10, 2003, interplanetary shock at 8.7 AU, *Geophys. Res. Lett.*, *32*, L17103, doi:10.1029/2005GL023079.

Wilson, L. B., III, C. Cattell, P. J. Kellogg, K. Goetz, K. Kersten, L. Hanson, R. MacGregor, and J. C. Kasper (2007), Waves in interplanetary shocks: A Wind/WAVES study, *Phys. Rev. Lett.*, *99*(4), 041101, doi:10.1103/PhysRevLett.99.041101.

Wilson, L. B., III, C. A. Cattell, P. J. Kellogg, K. Goetz, K. Kersten, J. C. Kasper, A. Szabo, and M. Wilber (2010), Large-amplitude electrostatic waves observed at a supercritical interplanetary shock, *J. Geophys. Res.*, *115*, A12104, doi:10.1029/2010JA015332.

Zaslavsky, A., et al. (2012), Interplanetary dust detection by radio antennas: Mass calibration and fluxes measured by STEREO/WAVES, *J. Geophys. Res.*, *117*, A05102, doi:10.1029/2011JA017480.